Waterborne Hyperbranched Polyurethane/Carbon Dot Nanocomposite

Highlight

Advanced applications of polymers urge development of novel materials with unique properties. Thus, the current chapter describes *in situ* and *ex situ* fabrication of tannic acid based waterborne hyperbranched polyurethane nanocomposites by incorporating three different weight percentages (0.5, 1.0 and 1.5 wt%) of carbon dot. Carbon dot was synthesized by using corms of *Colocasia esculenta* as the raw material. These fabricated nanocomposites were modified with 20 wt% of glycerol based hyperbranched epoxy and 10 wt% of fatty acid based poly(amido amine). FTIR, Raman, UV-visible, XRD and TEM analyses confirmed the structural changes occurred upon interaction of carbon dot with waterborne hyperbranched polyurethane matrix. The nanocomposites exhibited good photo luminescent behavior. Further, a dose dependent improvement of mechanical properties (tensile strength ~1.7 fold, elongation at break ~1.5 fold and toughness ~2.6 fold compared to pristine polymer) as well as thermal stability (maximum 20 °C enhancement) was witnessed. These nanocomposite films were found cytocompatible for *in vitro* adhesion, proliferation and differentiation of MG63 osteoblast cell line. Further, nanocomposite films with carbon dot loading of 1-5 wt% were tested for photo-catalytic activity by carrying out solar driven hydrogen peroxide preparation from water, ethanol and oxygen.

Parts of this chapter are published/communicated in

1. **Gogoi, S.**, Kumar, M., Mandal B.B., & Karak, N. High performance luminescent thermosetting waterborne hyperbranched polyurethane/carbon quantum dot nanocomposite with in vitro cytocompatibility, *Compos. Sci. Technol.* **118**, 39--46, 2015.

2. **Gogoi, S.**, & Karak, N. Solar driven hydrogen peroxide production using polymer supported carbon dot as heterogeneous catalyst, *Catal. Commun.* (Communicated).

4.1. Introduction

As discussed in Chapter 1, nanotechnology based polymeric composites have paved a new paradigm to material research owing to their huge viability for a wide range of advanced applications.[1-5] It has been observed that incorporation of even a minute quantity of nano-filler can lift up the various material properties dramatically.[6] The substantial differences in physico-chemical properties between nanomaterial and bulk phase lead to the unique behavior of the former, which can be explored to design polymeric nanocomposites with tunable properties.[7] Therefore, the present study made an effort to fabricate nanocomposites of tannic acid based waterborne hyperbranched polyurethane (WHPU) in order to enhance its various properties.

Among the various nanostructures, carbon-based nanomaterials have drawn copious attraction by virtue of tunable physical, chemical, electrical and biological properties.[8] Most recently, carbon dot (CD) has shown remarkable promises in this regard.[9] CD is the most recent addition to the carbonaceous nanomaterial family, which possesses dimension less than 10 nm. The most exciting properties of CD are excellent nano state aqueous solubility, excitation wavelength dependent stable multi-color emission and profound biocompatibility.[10-12] The phenomenal properties of CD, primarily attributed to quantum confinement effect confer it a special niche in domains ranging from biomedical, photocatalytic to optoelectronic applications.[13-16] Moreover, CD provides 'Green' preparative route by using nontoxic chemicals, environmentally benign solvents and largely available bio-based carbon raw materials.[9,17] CD, thus, appears to be a suitable candidate amidst all other, especially to design polymeric nanocomposites for biological, optical and photocatalytic applications.

Henceforth, the present chapter describes *in situ* and *ex situ* fabrications of WHPU/CD nanocomposites. As described in Sub-Chapter 2B, developed WHPU by virtue of attributes like low VOC content, bio-based origin and profound bioactivity has the prospective to address a cocktail of challenges ranging from sustainability to environmental footprints. Therefore, judicious inclusion of CD and WHPU onto the same matrix appears to pave direction towards the development of a sustainable material with exciting properties. The approach of using CD to fabricate WHPU seems to credit several advantages. The aromatic carbonized structure of CD with highly

polar peripheral groups may confer a strong physico-chemical interaction with the polymer matrix, which can lead to the enhancement of mechanical properties. On the other hand, quantum size dimension and good compatibility with the polymer matrix may help to retain transparency of the pristine film, which is difficult to achieve with other carbonaceous nanostructures. The optical emission under different wavelengths of UV light may help to design different optoelectronic devices, e.g. light emitting diode, UV detector or anti-counterfeiting material.[18,19] Considering the biological attributes, CD has the potentiality to promote biocompatibility of the nanocomposite system for allied biomedical applications. Likewise, by virtue of its photo-harvesting activity, such composite material can be used as photo-catalyst.

Considering all these facts, the present chapter made an effort to evaluate the fabricated system as a high performing, transparent and photo-luminescent polymeric material. The nanocomposite system was examined as an anti-counterfeit material. To highlight its biological properties, cytocompatibility, cell proliferation and differentiation tests were carried out with human osteoblast (MG63 cell line). Polymeric nanocomposite was further used as a photo-catalyst in solar driven production of hydrogen peroxide using water, ethanol and oxygen as raw materials. Thus, overall objective of the present study is to explore the potentiality of CD as a nano-filler to design polymeric nanocomposites with multifunctional properties.

4.2. Experimental

4.2.1. Materials

IPDI, PEG 600 and BD of similar grade and specifications were used as described in Sub-Chapter 2A (Section 2A.2.1.). Other chemicals used in the fabrication of WHPU/CD nanocomposite were BMPA, TA, TEA and THF. All these chemicals possessed similar grade and specifications as described in Sub-Chapter 2B (Section 2B.2.1.). Same type of bacterial culture of *P. aeruginosa* as mentioned in Sub-Chapter 2A, Section 2A.2.1. was used for biodegradation study. Similarly, same HE and PAA as mentioned in Chapter 3 (Section 3.2.1.) were used in the modification of nanocomposite films. Corms of *Colocasia esculenta (C. esculenta)* used in the synthesis of CD was collected locally from Tezpur University campus, Tezpur, India. Quinine

sulfate (Sigma-Aldrich, USA) was used as the reference compound for the determination of quantum yield of CD and nanocomposite films.

On the other hand Alamar Blue (Invitrogen, USA), Minimum Essential Medium (MEM, Gibco, USA), 10% fetal bovine serum (FBS, Gibco, USA), phosphate buffered saline (PBS, pH 7.4, Hi-Media, India), Live/Dead assay kit (Sigma-Aldrich, USA), calcein-AM (Sigma-Aldrich, USA), ethidium homodimer (Sigma-Aldrich, USA), β-glycerol phosphate disodium salt pentahydrate (Sigma-Aldrich, USA), L-ascorbic acid (Sigma-Aldrich, USA), dexamethasone (Sigma-Aldrich, USA), Alizarin Red S (Sigma-Aldrich, USA) and neutral buffered formalin (NBF, Sigma, USA) were used in the biological evaluation of the nanocomposite films. MG63 (human osteosarcoma) cell line was obtained from National Centre for Cell Science (NCCS), Pune, India.

Ethanol (C_2H_5OH, Merck, India), millipore water (H_2O, obtained from MilliQ® Ultrapure Water Solutions, Type 1, water purifier system) and oxygen (O_2, obtained from Jainex Gas Company, Guwahati, Assam, India) were used in the photo-catalytic production of hydrogen peroxide. Potassium permanganate ($KMnO_4$, Merck, India) was used in the quantitative estimation of hydrogen peroxide following a titrimetric method.

4.2.2. Characterization

FTIR spectra of the nanomaterial and nanocomposite were recorded under the same condition using the same spectrometer as stated in Sub-Chapter 2A (Section 2A.2.2.). Same photo-spectrometer was used to obtain UV-visible spectra of CD and WHPU/CD nanocomposite as described in Sub-Chapter 2B (Section 2B.2.2.). The shape and size of CD, as well as its distribution over the polymer matrix were visually studied by using High Resolution Transmission Electron Microscopic (HRTEM) analysis. TEM images were obtained from JEOL, JEMCXII, Japan, microscope at an operating voltage of 200 kV, using Cu grid of TED PELLA INC, Ultrathin C, Type A, 400 mesh. The microscopic data were analyzed for Fast Fourier Transform (FFT) and Inverse Fast Fourier Transform (IFFT) images by using Gatan Microscopy Suite Software. Elemental composition of CD was confirmed by Electron Dispersive X-ray study (EDX, Oxford, JSM-6390LV, UK). X-Ray Diffraction (XRD) patterns of CD and WHPU/CD nanocomposite were obtained by using Bruker AXS, Germany, Model: D8 Focus,

instrument (from $2\theta=10°-70°$ at a scanning rate of $2°$ min^{-1}). Graphitic structure of CD was studied with the help of Raman spectrometer, Renishaw, UK, Model: Renishaw Basis Series, using laser of wavelength 514 nm. Photoluminescence (PL) behavior was studied by using a PerkinElmer, USA, Model: LS-55 fluorescence spectrometer. For the evaluation of thermal and mechanical properties, the same instruments and instrumentation techniques such as TGA, DSC, UTM, scratch hardness tester, gloss meter, impact tester etc. were used as described in Sub-Chapter 2A (Section 2A.2.2.). Biodegraded polymeric films were studied by using the same SEM as mentioned in Sub-Chapter 2A (Section 2A.2.2.). On the other hand, fluorescence microscope EVOS FL, Life Technologies, USA was used in the Live/Dead assay. Multimode reader provided by Tecan, Infinite M200, Switzerland was used to measure absorbance values in the Alamar Blue assay.

4.2.3. Methods

4.2.3.1. Synthesis of CD

CD was synthesized by heating the aqueous extract of corms of *C. esculenta*. Briefly, 50 g of *C. esculenta* corm was cut into small pieces and grinded into paste by mixing with 150 mL of distilled water. The mixture was filtered thoroughly. Then 25 mL of the aqueous extract was mixed with 25 mL of ethanol. Mixture was heated at 150 °C for 3.5 h in a conical flask sealed with a cotton plug almost to dryness. The soluble fraction of the dark brown colored residue was dissolved in 25 mL of distilled water and separated by filtration. In order to separate the large particles, 50 mL of ethanol was added to the filtrate and centrifuged at 3000 rpm (1006×g) for 15 min. Water was removed under reduced pressure to get the nanoparticles. CD, thus obtained was stored in a vacuum desiccator. CD was also prepared by a hydrothermal method subjecting aqueous extract of corms of *C. esculenta* into a hydrothermal condition by using a Teflon lined autoclave at 150 °C for 8 h. CD obtained through hydrothermal method was used in photo-catalytic reaction.

4.2.3.2. Fabrication of WHPU/CD nanocomposite

WHPU/CD nanocomposite was fabricated by following both *in situ* and *ex situ* techniques. For *in situ* fabrication, required amount of IPDI, PEG 600 and BMPA (maintaining -NCO to -OH ratio 1.5) were reacted at 80±2 °C for 1.5 h inside a glass

reactor equipped with a condenser, a nitrogen gas inlet and a mechanical stirrer. In the next step, THF solution of BD and TA were added so that -NCO/-OH ratio became 1.1 and further reaction was carried out at 70±2 °C for another 3.5 h. This was followed by addition of CD and BD to the reaction mixture by adjusting -NCO/-OH ratio 1 and reaction was continued for another 1.5 h. Then the reaction was stopped and temperature was allowed to fall. When temperature reached near about 25 °C, -COOH groups were neutralized by adding TEA. Finally, water was added at a very slow rate with constant stirring. THF was recovered under reduced pressure. All the steps were carried out under the inert atmosphere of nitrogen with constant mechanical agitation. Different weight percentages of CD, *viz.* 0.5, 1.0 and 1.5 wt% were used to prepare different compositions of the nanocomposite, which were coded as PNC0.5, PNC1.0 and PNC1.5, respectively. To prepare the nanocomposite films, these compositions were mixed with 20 wt% of HE and 10 wt% PAA by ultra-sonication, which were then cast on glass plates, dried under atmospheric condition and heated at 100 °C for 45 min. Films were finally peeled out by warming in hot water. For *ex situ* fabrication, the same method was employed except CD was introduced in the modification step instead of incorporating it during the polymerization reaction. The nanocomposite films thus obtained were dried at 50 °C for 3 h in an oven. They were kept inside a desiccator and used for various studies. A pristine system was also prepared which is equivalent to MWPU20 as described in Chapter 3. However a general coding MWPU has been used in this chapter.

4.2.3.3. Quantum yield

Quantum yield of CD and PNCs was determined by using the following formula:[17]

$$Q_{Sample} = Q_{R} \frac{I_{Sample}.A_{R}.\eta^2_{Sample}}{I_{R}.A_{Sample}.\eta^2_{R}} \ldots\ldots\ldots\ldots\ldots\ldots\ldots\ldots\ldots\ldots.(\textbf{Eq. 4. 1})$$

where Q_{Sample} is the quantum yield of the test sample, Q_{R} is the quantum yield of the reference compound, I_{Sample} is the luminescence intensity of the test sample, I_{R} is the luminescence intensity of the reference compound, A_{Sample} is the absorbance of the test sample at excitation wavelength, A_{R} is the absorbance of the reference compound at excitation wavelength and η is the refractive index of the solvent used. In the present study quinine sulfate was used as the reference compound. All the luminescence intensity and absorbance were measured at wavelength of 360 nm.

Quantum yield of quinine sulfate at 360 nm is 54%. Water was used as the solvent for both CD and quinine sulfate.

4.2.3.4. HOMO-LUMO band gap

The band gap of CD was evaluated from UV-visible spectroscopy by using the following equation:[20]

$$\alpha = \frac{C(h\nu - E_{bulk})^{1/2}}{h\nu} \dots \dots \dots \dots \dots \dots \dots \dots \dots \dots \dots . . (Eq. 4.2.)$$

here, α is the absorption coefficient, C is constant, h is Plank's constant, ν is the frequency and E_{bulk} is the energy gap. In practice, band gap is calculated by plotting $h\nu$ versus $(\alpha h\nu)^2$. The extrapolation of the curve to $(\alpha h\nu)^2$ gives the value of E_{bulk}.

3.2.3.5. Biodegradation

Bacterial biodegradation study was carried out according to the method described in Sub-Chapter 2A (Section 2A.2.3.4.) using bacterial culture of *P. aeruginosa*.

4.2.3.6. Cell proliferation and osteogenic differentiation assay

(a) *Cell culture and Alamar Blue cell proliferation assay*

MG63 human osteosarcoma cells were cultured in MEM supplemented with 10% FBS and and penicillin streptomycin (1x). Cells were maintained at 37 °C in a humidified incubator with 5% CO_2. Medium was replenished twice a week. For cell proliferation study, polymeric nanocomposite membranes were sterilized by autoclaving and pre-conditioned in complete MEM for overnight. Cells were cultured on the films (having diameter of 10 mm) of all the four variants, *viz.* MWPU, PNC0.5, PNC1.0 and PNC1.5 (*in situ*). Each film was seeded with 5×10^4 cells and cultured for 9 days. Cell proliferation was examined by Alamar Blue at day 1, 6 and 9 following the manufacturers' protocol (n=4). Alamar Blue is a non-toxic dye, which measures the viability and proliferation of the same batch of seeded cells at different time points. Briefly, cell seeded films were incubated in medium supplemented with 10% (v/v) Alamar Blue dye for 3 h. After incubation, 100 μL of the medium from each sample was collected and absorbance was measured at 570/600 nm in a multimode reader. Films without cells supplemented with 10% Alamar Blue dye were used as the negative control.

(b) Live/Dead assay

For Live/Dead assay, cells were seeded on the polymeric films (MWPU, PNC0.5, PNC1.0 and PNC1.5 (*in situ*)) and analyzed for their viability and adherence after 7 days of culture. Viability of the cells was assessed by using Live/Dead assay. Briefly, films were rinsed with PBS and incubated in a solution of 4 μM calcein AM and 2 μM ethidium homodimer prepared in PBS to stain live and dead cells, respectively. After 15-20 min of incubation at 37 °C, films were washed with PBS and then visualized under a fluorescence microscope. Viable cells converted calcein AM to calcein which produced green fluorescence. Dead cells were monitored by ethidium homodimer binding to DNA, which entered into the dead cells through damaged cell membrane and produced red fluorescence.

(c) Osteogenic differentiation

Nanocomposite films were evaluated for osteogenic differentiation of MG63 in osteogenic media. Cells were cultured on pre-conditioned films in differentiation medium comprising of MEM supplemented with 10 mM disodium-β-glycerol phosphate, 50 μg mL^{-1} L-ascorbic acid and 10^{-8} M dexamethasone.[21,22] The calcium deposition was monitored by using Alizarin Red S stain (2% w/v, pH 4.1-4.3). Cell-seeded membranes were fixed in 10% NBF for overnight rinsed in distilled water followed by staining with Alizarin Red S solution for 2 min. Excess stain was removed by washing. The membranes were dipped in acetone and acetone-xylene solution. Images were taken under bright field microscope (n=3).

4.2.3.7. Photo-catalytic activity

The developed nanocomposite was tested for its photo-catalytic activity for a solar driven preparation of H_2O_2 using H_2O, C_2H_5OH and O_2 as raw materials. A series of nanocomposites was prepared according to the method described in section 4.2.3.2. by using five different weight percentages of CD, i.e. 1.0, 2.0, 3.0, 4.0 and 5.0 wt%, which were designated as PNC1.0, PNC2.0, PNC3.0, PNC4.0 and PNC5.0, respectively. H_2O, C_2H_5OH (100%) and mixtures of H_2O and C_2H_5OH (25%, 50% and 75% (v/v)) were used as starting materials. The reactants were taken inside a two neck glass reactor, which was made saturated with molecular O_2 and then sealed. Then it was irradiated under normal solar light with intensity of ~70,000-80,000 lux at ca. 25 °C

temperature for different time intervals. The production of H_2O_2 was estimated by redox titration method using $KMnO_4$.[23]

4.3. Results and discussion

4.3.1. Synthesis and characterization of CD

CD was synthesized by heating the aqueous extract of corms of *C. esculenta* as a carbohydrate rich bio-precursor. It contains various carbohydrates like glucose, fructose, sucrose, ascorbic acid etc.[24] It is believed that CD was formed by the carbonization of these carbohydrates under hydrothermal or even simple heating condition.[17,25,26] De and Karak tried to depict the plausible mechanism of CD formation from such carbohydrate rich bio-resources.[17] Accordingly, it has been proposed that in the initial phase hydrolysis, dehydration and decomposition took place to from soluble compounds like furfural aldehyde and ketones along with several other organic acids such as acetic, levulinic, formic acid etc. In the next step, polymerization and condensation of these compounds resulted in the formation of soluble polymeric products. Then extensive aromatization and carbonization occurred *via* cycloaddition and condensation reaction. CD was ultimately formed at a critical concentration by nuclear burst of these aromatic clusters. The morphology of the synthesized CD was studied by TEM analysis (**Figure 4.1a**). The TEM image
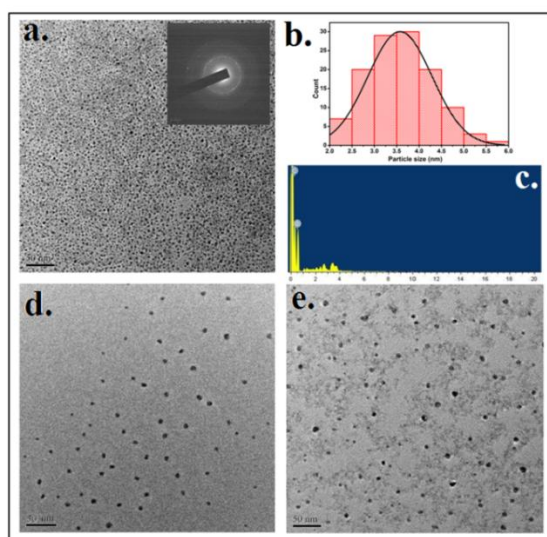
Figure 4.1. (a) TEM image of CD (inset SAED pattern), **(b)** Particle size distribution of CD, **(c)** EDX spectrum of CD, **(d)** TEM image showing distribution of CD in PNC1.5 (*ex situ*) and **(e)** TEM image showing distribution of CD in PNC1.5 (*in situ*).

depicted in the figure confirmed the formation of carbon nanoparticles with almost spherical shape, having dimension in the 2.2-5.1 nm range. Statistical evaluation of size distribution (**Figure 4.1b**) revealed that the mean size of the particles was 3.2 nm. However, in hydrothermal method a more restrained size distribution was observed in the range of 1.5-2.8 nm. HRTEM micrographs showed a lattice spacing of 0.341 nm which is close to the (002) lattice spacing of graphitic carbon (**Figure 4.2a** and **d**). The Raman spectrum of CD exhibited two distinct bands, *viz.* D and G bands at 1362 and 1582 cm^{-1}, respectively as shown in **Figure. 4.3a (i)**. The appearance of D band indicates the presence of disorder in the graphitic structure. Such disorder originates from the presence of different oxygen functional groups present in CD. However, I_D/I_G ratio (0.57) indicates the formation of near pristine graphitic structure in the form of CD. The 2D peak at 2765 cm^{-1} can be ascribed to the multilayered structure of CD. On the other hand, XRD pattern showed a broad peak at around 2θ value of 23.5° (**Figure 4.3b (i)**), which indicates higher interlayer spacing and poor crystallinity of CD compared to pristine graphitic carbonaceous structure. Generation of oxygenous groups contributed towards amorphous behavior of CD. Characteristic FTIR absorption frequencies at 3465, 2975, 1680, 1602, 1542 and 1246 cm^{-1} confirmed the presence of -O-H, -C-H, -C=O, -C=C- and -C-O-C- groups,
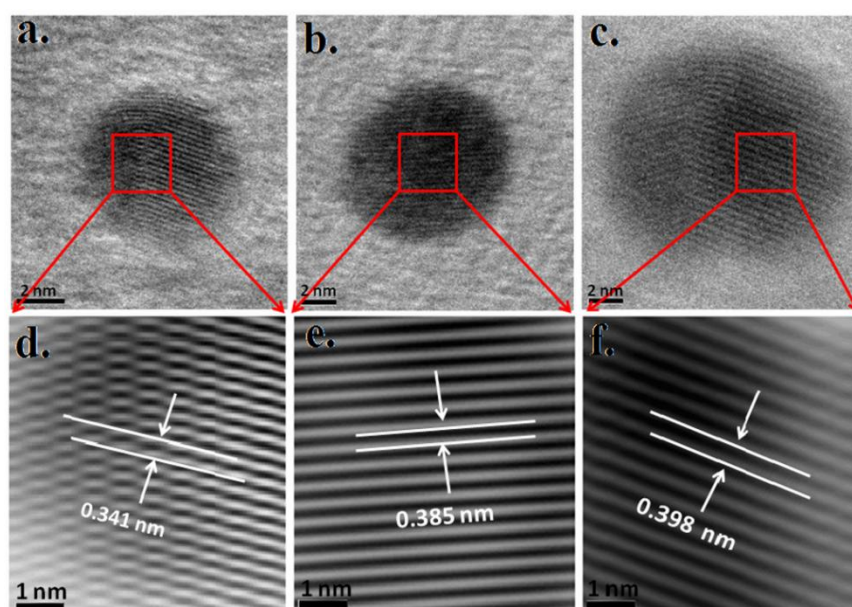
Figure 4.2. HRTEM images of **(a)** CD, **(b)** PNC1.5 (*ex situ*) and **(c)** PNC1.5 (*in situ*); Corresponding IFFT images of **(d)** CD, **(e)** PNC1.5 (*ex situ*) and **(f)** PNC1.5 (*in situ*).
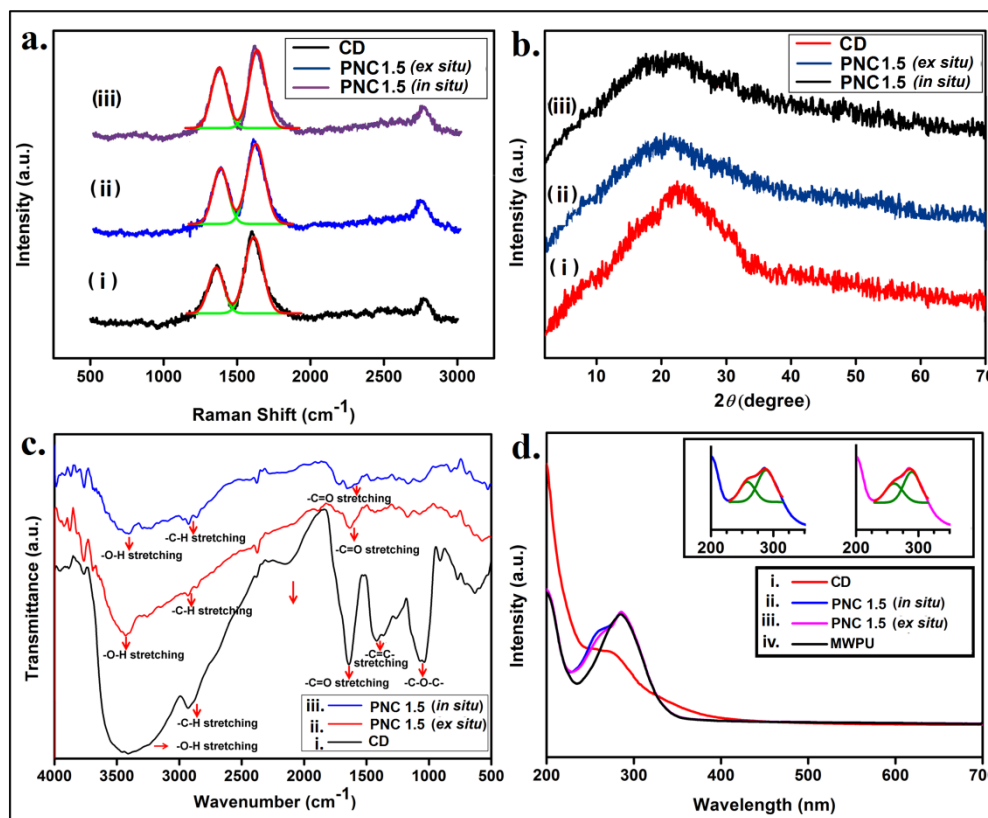
Figure 4.3. (a) Raman spectra of (i) CD, (ii) PNC1.5 (*ex situ*) and (iii) PNC1.5 (*in situ*); **(b)** XRD patterns of (i) CD, (ii) PNC1.5 (*ex situ*) and (iii) PNC1.5 (*in situ*); **(c)** FTIR spectra of (i) CD, (ii) PNC1.5 (*ex situ*) and (iii) PNC1.5 (*in situ*); **(d)** UV-visible spectra of (i) CD, (ii) PNC1.5 (*in situ*) and (iii) PNC1.5 (*ex situ*) and (iv) MWPU (inset deconvoluted spectra of PNC1.5 (*ex situ*) and PNC1.5 (*in situ*)).

respectively (**Figure 4.3c (i)**). Elemental analysis of CD showed the presence of C and O in a weight ratio of 61.47:36.53 (**Figure 4.1c**). In the UV-visible spectrum, an absorption peak at around 265 nm was observed for CD (**Figure 4.3d (i)**), which was considered as the indication for CD formation.[27]

4.3.2. Fabrication and characterization of WHPU/CD nanocomposite

Different compositions of WHPU/CD nanocomposite, i.e. PNCs were fabricated by *in situ* as well as *ex situ* polymerization techniques using 0.5, 1.0 and 1.5 wt% of CD as mentioned in section 4.2.3.2. Different chemical functionalities present were established by FTIR spectroscopy as depicted in **Figure 4.3c** (**ii** and **iii**). Various oxygen functional groups of CD possess an inherent tendency to interact with WHPU or WHPU precursors by either covalently or non-covalently as shown in **Scheme 4.1**.
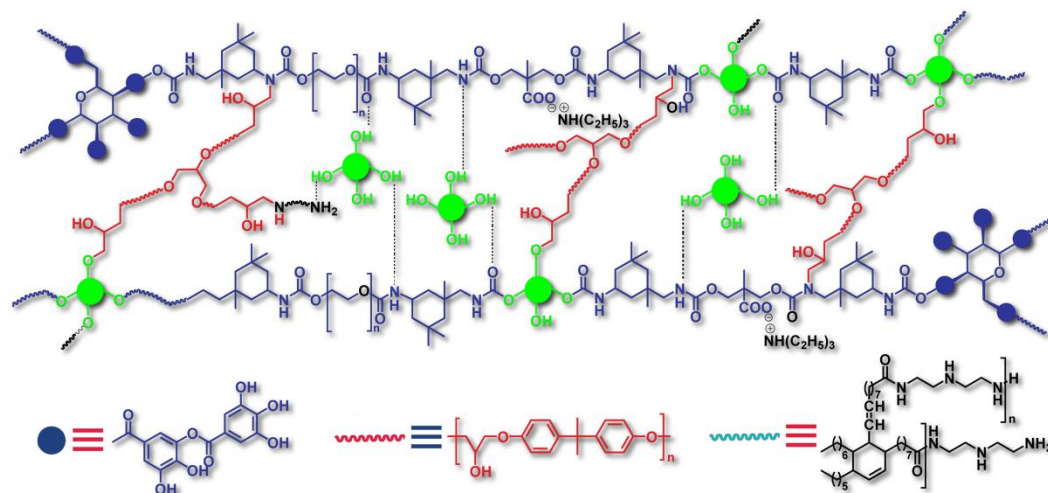
Scheme 4.1. *In situ* fabricated WHPU/CD nanocomposite (for *ex situ* WPHU/CD nanocomposite covalent interaction of CD with the polymer matrix are not present).

Such interactions played the central role to achieve a homogeneous distribution of the nanomaterial over the polymer matrix. In many instances, lack of proper solubility and functionality of nanomaterial and polymer create barrier to form a homogeneous nanocomposite system. In this context, use of CD and WHPU is an apt option because of their excellent dispersibility in aqueous phase. TEM images of PNC1.5 depicted in **Figure 4.1d** and **e** confirmed a uniform sharing of CD even at the high nanomaterial loading (1.5 wt%). HRTEM and corresponding IFFT images (**Fig. 4.2a-f**) revealed that the layer spacing of CD increased after fabrication, which was more pronounced for *in situ* PNC1.5 (0.398 nm) compared to the *ex situ* counterpart (0.385 nm). This might arise due to intercalation of polymeric chains in between the layers of CD. Raman spectra of PNC1.5 (*ex situ* and *in situ*) as shown in **Figure 4.3a** (**ii** and **iii**) displayed both D and G bands at 1344 and 1589 cm^{-1} similar to that of CD. However, the most obvious difference marked was the increased intensity of D band compared to the same of pristine CD. This originated from the additional defect or disorder created in CD structure during the fabrication of nanocomposites. This implied definite interaction between CD and the WHPU matrix. The XRD pattern of PNC1.5 (*ex situ* and *in situ*) followed a much weakly intense and broad peak as shown in **Figure 4.3b** (**ii** and **iii**). The UV-visible spectra of PNCs depicted in **Figure 4.3d** (recorded before modification) showed a doublet. Deconvolution of the same gives the idea about the existence of two overlapping peaks; the intense peak at 280 nm is

for catechol fraction of the polymer, while slightly weakly intense peak at 265 nm is for CD (inset to the **Figure 4.3d**).

4.3.3. Mechanical properties

Various mechanical properties of PNCs are presented in **Table 4.1**. From the results, we witnessed an excellent enhancement of mechanical properties of the nanocomposite even at a low loading of CD compared to WHPU and MWPU. The major drawbacks of epoxy modified PU are the decrease in elongation at break value and loss of flexibility. In the current study we witnessed ~44% decrease in elongation at break value of the pristine polymer after modification (comparing with the data presented in Chapter 3, Section 3.2.2.). But, significantly this property was improved after the formation of nanocomposite by 1.6 fold (maximum). This may originate from the layered structure of CD. A dose dependent enhancement of tensile strength was also perceived by the fabrication of the nanocomposite. PNCs exhibited high

Table 4.1. Mechanical properties of PNCs

Composition		TS (MPa)	E@B (%)	Toughness§ (MPa)	SH† (kg)	IR‡ kJ m^{-1}	Gloss (@60°)
		Mechanical property*					
WHPU¶		6.0±0.2	457±3	19.36	5.0±0.2	6.64±0.13	94.5±0.8
MWPU¶		17.0±0.5	220±2	28.74	9.0±0.2	8.25±0.12	95.2±0.3
In situ	PNC0.5	19.4±0.2	265±3	47.66	9.5±0.3	8.28±0.15	96.7±0.5
	PNC1.0	25.4±0.3	289±2	63.49	>10	>8.30	96.9±0.6
	PNC1.5	28.5±0.2	340±3	75.51	>10	>8.30	98.4±0.7
Ex situ	PNC0.5	17.9±0.4	245±3	36.85	9.5±0.2	8.27±0.12	95.4±0.4
	PNC1.0	20.4±0.3	262±1	44.62	>10	>8.30	96.8±0.5
	PNC1.5	23.4±0.2	305±3	55.53	>10	>8.30	97.4±0.3

*Mechanical properties: TS=Tensile strength, E@B=Elongation at break, SH=Scratch hardness, IR=Impact resistance; §Obtained by calculating area under stress-strain curve; †Limit of scratch hardness tester was 10 kg (maximum); ‡Limit of impact tester is 8.30 kJ m^{-1} for film of thickness 1mm (maximum); ¶Data reproduced from earlier chapters (Sub-Chapter 2B and Chapter 3) for comparison.

values of scratch hardness and impact resistance. However, we could not quantify the exact values as both scratch hardness and impact resistance crossed the limiting values of the instruments used. Nevertheless, measurement of toughness clearly showed an excellent gain in mechanical performance after the formation of nanocomposite. The improved performance of PNCs can be attributed to the factors such as excellent dispersion, strong interfacial interactions and nano scale morphology of CD. CD with carbonized core structure and large peripheral polar functional groups can provide stiffness and strong interactions within the polymer matrix, which played the vital role towards the improved mechanical properties of PNCs. On the other hand, *in situ* PNCs exhibited better mechanical properties than the *ex situ* ones by virtue of better dispersion and strong interactions as discussed in Section 4.3.2. Similar type of enhancement in mechanical properties was achieved by De *et al.* for a hyperbranched epoxy/CD nanocomposite system.[28]

4.3.4. Thermal properties

In order to evaluate the thermal stability of PNCs, TG study was conducted. We found improved thermo-stability after the formation of the nanocomposite (**Figure 4.4**), which was consistent with the loading of CD. The increased thermo-stability of the nanocomposites can be attributed to high cross-linking density and secondary
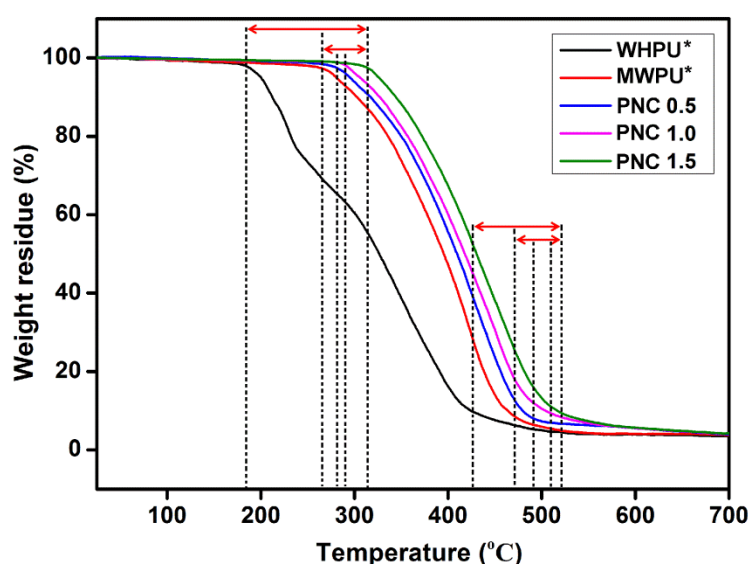
Figure 4.4. TG thermograms of PNC0.5, PNC1.0 and PNC1.5 (*in situ*). *Data reproduced from Sub-Chapter 2A and Chapter 3 for comparison.

interactions imparted by CD with the polymer chains. In a highly cross-linked network, molecular chain excitation and motion generated during exposure to thermal energy is prohibited significantly, which makes the degradation process energy consuming.[29] CD by virtue of large number of functional groups participated in the chemical cross-linking reaction (**Scheme 4.1**). This imparted restrictions in the macromolecular chain motion making the system more rigid. Consequently, the process of bond breaking became more heat expensive resulting greater thermo-stability of nanocomposites compared to MWPU and WHPU. Secondary interactions like H-bonding and polar-polar interactions also played a vital role towards the enhancement of thermal properties as discussed in Chapter 3 (Section 3.3.4.).

4.3.5. Optical properties

The nanocomposite possessed fascinating optical properties. All the compositions exhibited good transparency, which is difficult to achieve with other carbonaceous nanomaterials (**Figure 4.5a** and **b**). This can be attributed to the quantum size of the nanoparticles and their excellent dispersion in the polymer matrix. On the other hand, change in color of both CD and nanocomposite films were examined under visible, short UV (254 nm) and long UV (365 nm) region. The original light brown color of CD changed into green and deep blue under the exposure of long and short UV light, respectively (**Figure 4.6d**). Similar color change was perceived in case of PNC films as well (**Figure 4.6f** and **g**). Detail optical properties of CD and PNCs were
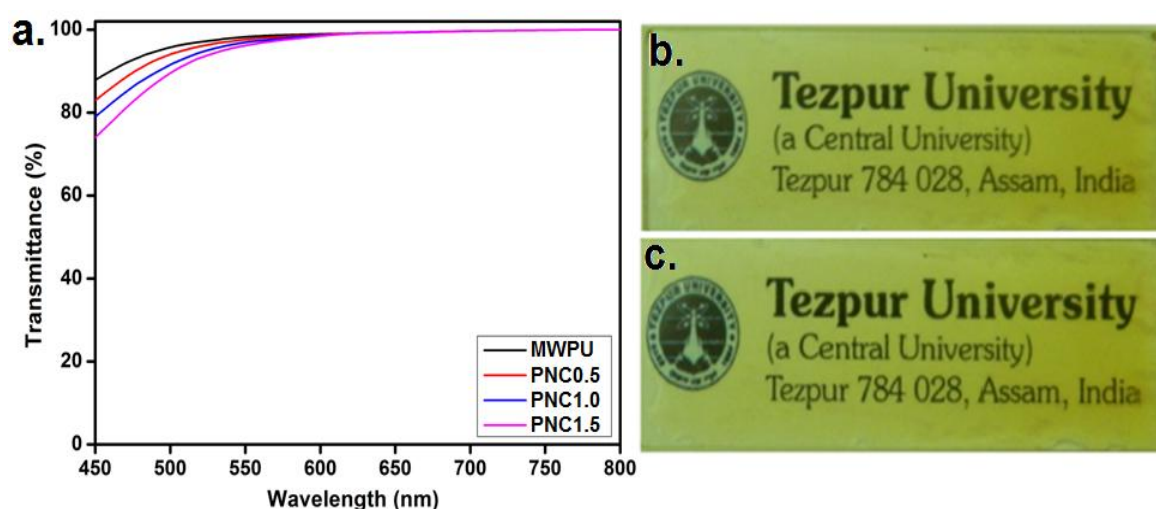

Figure 4.5. (a) % Transmittance of PNCs (*in situ*), **(b)** PNC1.5 (*in situ*) film showing transparency and **(c)** PNC1.5 (*ex situ*) film showing transparency.

studied by PL spectroscopy as depicted in **Figure 4.6a-c**. An excitation wavelength dependent photoluminescence behavior was witnessed with shifting of the emission peaks towards higher wavelength compared to the excitation wavelength. This can be ascribed to the existence of different surface states and size dispersion of CD. Quantum   yields were found as 10.42, 7.97 and 6.82% for CD, PNC1.5 (*in situ*) and PNC1.5 (*ex situ*), respectively. The better quantum yield value of PNC1.5 (*in situ*) compared to PNC1.5 (*ex situ*) is due to better dispersion of CD in the former than in the later. In contrary to CD, a broad emission peaks were observed for the PNC films as depicted in **Figure 4.6b** and **c**. This can be attributed to the inner filter effect, which results from the re-absorption of emitted light in a condensed matter. Short wavelength light emitted by PNC may be absorbed by CD in the matrix. This may result re-emission of red shifted long wavelength light. This is a repeated process,
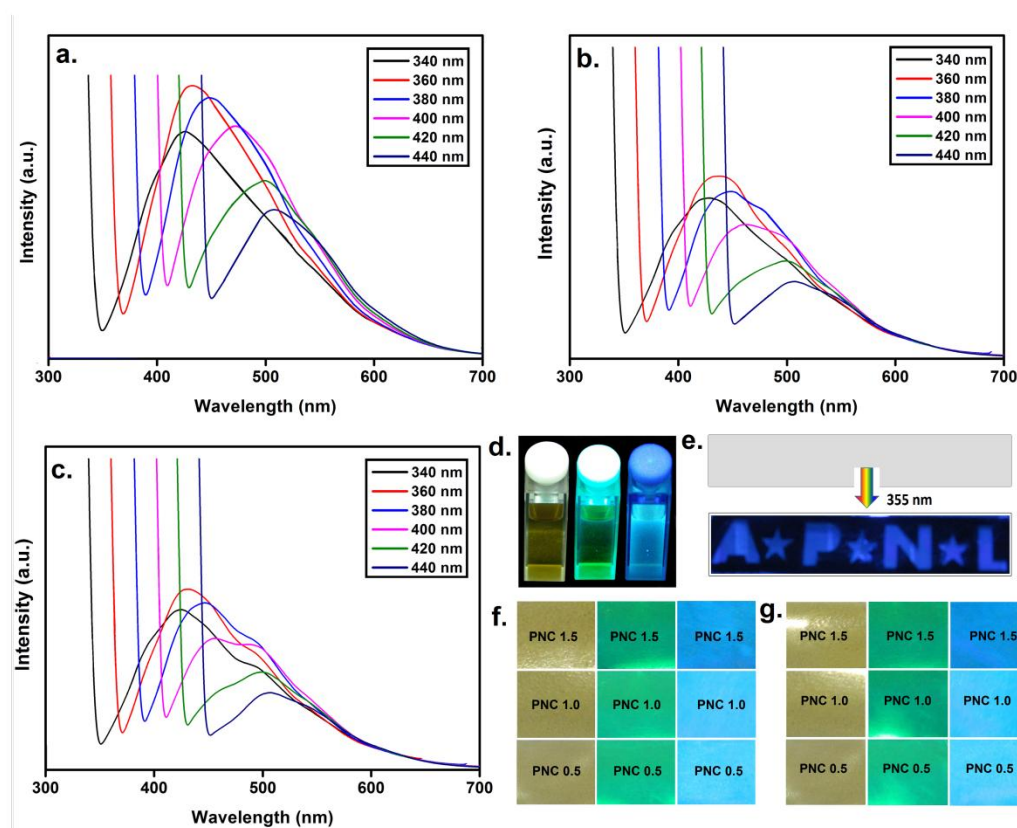
Figure 4.6. PL spectra of **(a)** CD, **(b)** PNC1.5 (*ex situ*) and **(c)** PNC1.5 (*in situ*); **(d)** Luminescence of CD under visible, short UV (254 nm) and long UV (365 nm); **(e)** Demonstration of PNC as a security mark; **(f)** and **(g)** Luminescence under visible, short UV (254 nm) and long UV (365 nm) of PNCs (*ex situ*) and PNCs (*in situ*).

which occurs until the emitted light passes through the film completely. This results the cut-off of short wavelength emission followed by enhancement of long wavelength emission. As a result, the PL intensity of the existing peaks gradually diminished and peaks at higher wavelength simultaneously evolved resulting in their broadening. In this vein, WHPU matrix seems to play an important role by providing mechanical support as well as uniform dispersion to prevent solid state quenching of CD. Moreover, similar to CD, PNC films also exhibited wavelength dependent emission and concentration dependent intensity. Such highly photoluminescent material can be used to fabricate novel engineered material for opto-electronic applications. **Figure 4.6e** demonstrates anti-counterfeiting application of the fabricated PNC.

4.3.6. Biological properties

4.3.6.1. Biodegradation

Bacterial degradation study of PNC films revealed adequate biodegradation over the experimental period of seven weeks. Weight loss profiles confirmed that fabrication of WHPU/CD nanocomposites offer a susceptible surface for bacterial adherence, resulting high weight loss over the experimental period, which was almost consistent with the nanomaterial loading in the polymer matrix (**Figure 4.7a**). Bacterial growth curves further support such observation (**Figure 4.7b**). An increasing trend in the
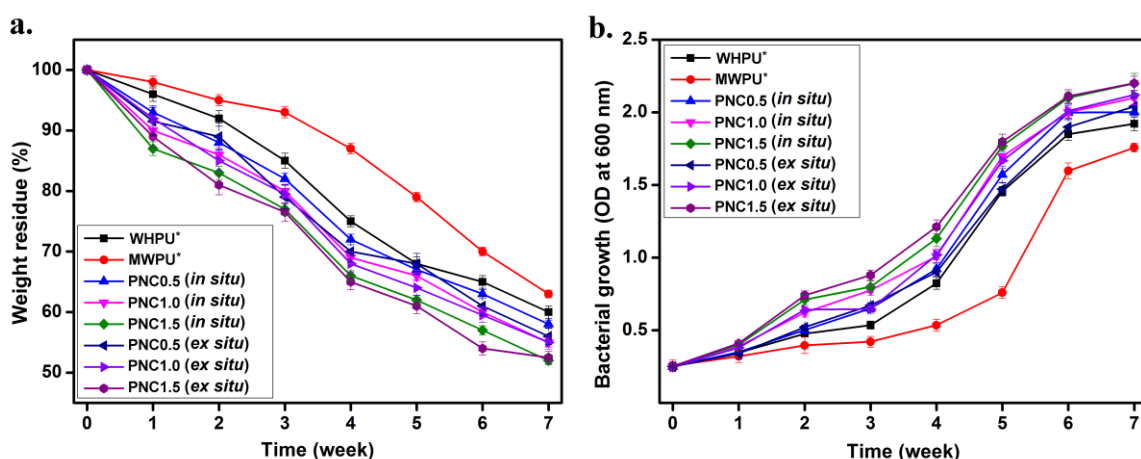

Figure 4.7. (a) Weight loss profiles of PNCs due to bacterial degradation and **(b)** Bacteria growth curves of *P. aeruginosa* on PNCs. *Data reproduced from Sub-Chapter 2B and Chapter 3 for comparison.

bacterial population was recorded with time. With increase in CD loading, rate of bacterial growth was also increased. SEM images (**Figure 4.8**) further confirmed significant bacterial adherence as well as surface erosion due to the bacterial exposure on the PNC films. Compered to WHPU and MWPU, the rate of bacterial degradation was found more in case of PNC films. Thus, the study denied any adverse effect of fabrication on inherent biodegradability of the original polymer system.
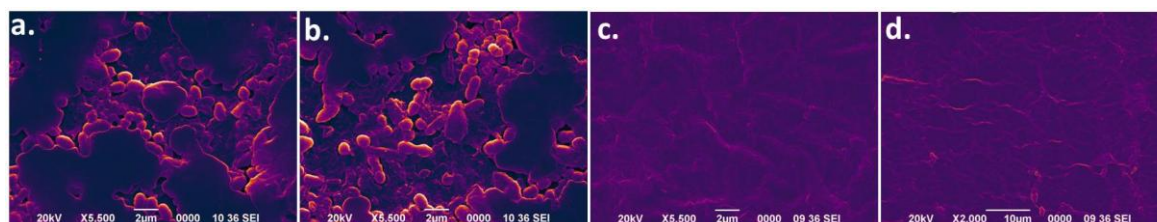

Figure 4.8. SEM images of **(a)** biodegraded PNC1.5 (*in situ*), **(b)** biodegraded PNC1.5 (*ex situ*), **(c)** PNC1.5 (*in situ*) before biodegradation and **(d)** PNC1.5 (*ex situ*) before biodegradation.

4.3.6.2. Cell proliferation and osteogenic differentiation assay

Cell proliferation assay was carried out with MG63 cell line in order to judge the potentiality of WHPU/CD nanocomposite as biomaterial. The observed Alamar Blue reduction values, which have a direct relationship with the cellular metabolism and cell proliferation at a given point of time suggest that the CD impregnated films are cytocompatible for biological application.[21,22] In comparison to day 1, Alamar Blue assay revealed ~20% increase in cell number on MWPU and PNC0.5, while ~30% increment was perceived on PNC1.0 and PNC1.5 after 9th day of culture (**Figure 4.9**). However, no statistical significance was observed between the groups (p>0.05). From the results it can be said that PU, a well reputed biomaterial, which is the main component of the PNC films aids to MG63 cell adhesion and proliferation.[30] Additionally CD, the other constituent of the nanocomposite films, which is known as a biologically active nanomaterial further enhances these bioactvities.[31,32] Incorporation of CD in WHPU leads to better cell proliferation on PNC1.0 and PNC1.5 compared to MWPU film. On the other hand, Live/Dead assay indicated attachment and viability of MG63 cells onto the nanocomposite membranes. Cells maintained their native morphology and were distributed uniformly on all the tested films (**Figure 4.10a**, **b**, **c** and **d**). Proliferating cells were found to form clusters on the
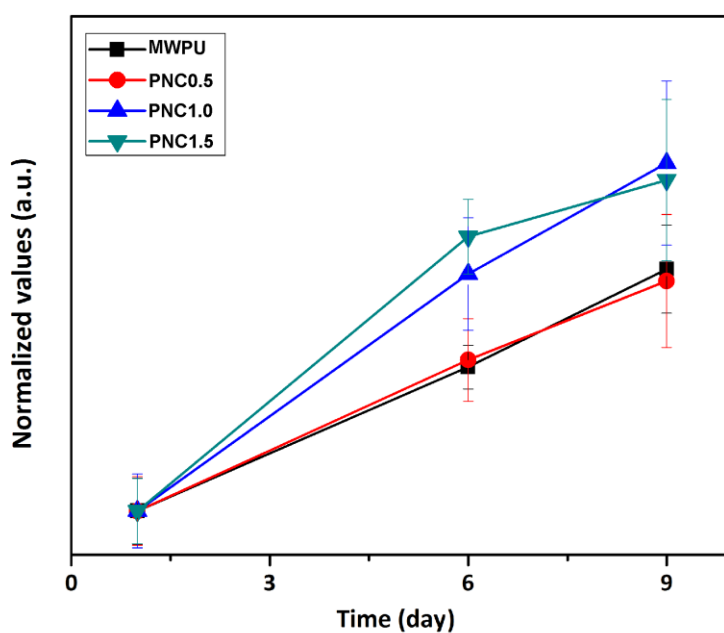
Figure 4.9. Alamar Blue cell proliferation assay showing MG63 osteosarcoma cell proliferation on WHPU and PNCs (*in situ*). Data represented as the average±standard deviation.

films, which is further expected to help in good cell to cell signaling leading to enhanced extracellular matrix (ECM) secretion and deposition. Enhancement of ECM formation is very important in the context of tissue engineering application, as high ECM would lead to mature tissues similar as in native state. Live/Dead result was found to be in agreement with the Alamar Blue cell proliferation results. This suggests cytocompatibility of the PNC films. Alizarin Red S staining was performed to confirm the hallmark characteristic of osteogenic differentiation, i.e. mineral deposition on the films. Films seeded with MG63 cells in osteogenic media for 10 days were assessed for calcium deposition. Microscopic analysis showed enhanced osteogenic differentiation on the films resulting extensive extracellular mineralization in the form of deposited nodules. Intense red Alizarin Red S staining of nodules all over the films confirmed extensive mineralization (**Figure 4.10 f, g, h** and **i**). These granules were formed in patches area of diffused and nodular mineralization throughout the films. **Figure 4.10e** and **j** indicate PNC1.5 films without cells. This clearly suggests suitability of WHPU/CD nanocomposite for bone tissue regeneration and other allied biological applications.
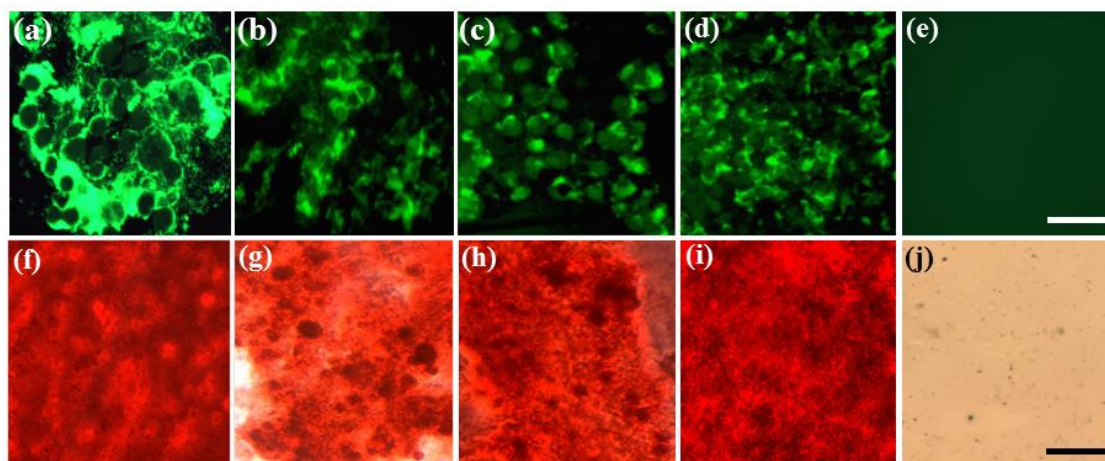
Figure 4.10. Fluorescent microscopic images showing MG63 cells growing on **(a)** MWPU, **(b)** PNC0.5, **(c)** PNC1.0 and **(d)** PNC1.5 (*in situ*) after seven days of culture; Light microscopic images of **(f)** MWPU, **(g)** PNC0.5, **(h)** PNC1.0 and **(i)** PNC1.5 (*in situ*) showing mineralized deposits in the form of nodule due to osteogenic differentiation of MG63 cells; Microscopic images **(e)** and **(j)** represent PNC1.5 (*in situ*) film without cell. Scale bar represents 100 μm.

4.3.7. Photo-catalytic activity

Fabricated nanocomposite films were used as heterogeneous photo-catalyst for solar driven H_2O_2 preparation. Use of CD in the form of polymeric nanocomposite helped to overcome certain difficulties, which otherwise would have been faced. These include separation of catalyst (CD is soluble in H_2O and C_2H_5OH) and solid state quenching of light harvesting activity (as mentioned in Section 4.3.3.). CD can act as a photo-catalyst for light-induced redox processes due to its electronic structure, which is characterized by a filled valence band and an empty conduction band. Absorption of a photon with energy greater than the band gap energy (E_{bulk}) leads to the formation of an electron and hole pair (e^- and h^+). In the absence of suitable scavengers, the stored energy is dissipated within a few nanoseconds by recombination. When C_2H_5OH was used, h^+ oxidized it into aldehyde and proton, while e^- promoted a two-electron reduction of O_2 to produce H_2O_2.[33,34]

$$CD \rightarrow e^- + h^+$$
$$CH_3 - CH_2 - OH + h^+ = CH_3 - CHO + 2H^+$$
$$O_2 + 2H^+ + 2e^- = H_2O_2$$
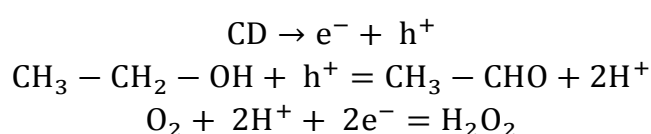
When H_2O was used as the raw material, h^+ oxidized H_2O into O_2. Similar two-electron reduction of O_2 was followed thereafter to produce H_2O_2 (**Scheme 4.2**).[33]

$$CD \rightarrow e^- + h^+$$

$$2H_2O + h^+ = O_2 + 4H^+$$

$$O_2 + 2H^+ + 2e^- = H_2O_2$$
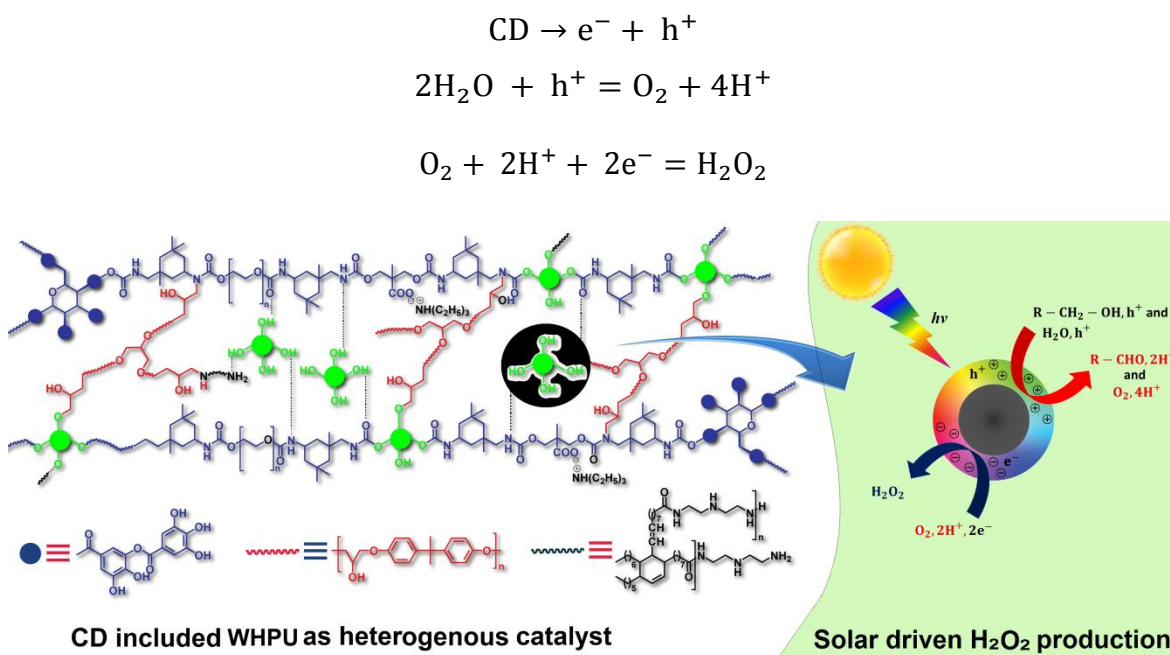
Scheme 4.2. Plausible mechanism for solar driven H_2O_2 production using PNCs (*in situ*).

Generally, splitting of H_2O requires the bottom level of the conduction band to be more negative than the redox potential of H^+/H_2 (0 V *vs* NHE), while the top level of the valence band should be more positive than the redox potential of H_2O/O_2 (1.23 V *vs* NHE).[32] Thus, the minimum value of E_{bulk} of any photo-catalyst should be 1.23 eV for H_2O splitting. However, for effective H_2O splitting the band gap should be larger than 2.0 eV. It is because, in real practice, loss of energy may happen due to kinetic over potential.[30] In the present study, E_{bulk} was evaluated as 2.21 eV for CD (**Figure 4.11**). Hence, it fulfils this criterion to act as a catalyst for solar driven production of H_2O_2. The study revealed that, PNC films effectively acted as photo-catalyst for the designed H_2O_2 preparation reaction. It was found that H_2O_2 production was less (~46 µM after 50 h of reaction) when only H_2O was used compared to the reaction with 100% C_2H_5OH (~82 µM). In case of C_2H_5OH/H_2O mixtures, H_2O_2 production increases with increase amount of C_2H_5OH in the mixture (~49 µM for 25%C_2H_5OH/75%H_2O, ~61 µM for 50%C_2H_5OH/50%H_2O and ~70 µM for 75%C_2H_5OH/25%H_2O).   This is
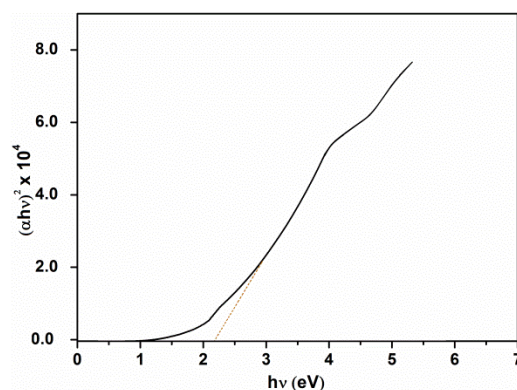
Figure 4.11. Plot of $(\alpha h\nu)^2$ *vs* $h\nu$.

shown in **Figure 4.12a.** The increased H_2O_2 production in the presence of C_2H_5OH can be ascribed to favorable thermodynamic driving force, which is promoted by suitable oxidation and reduction potential value of the catalyst when C_2H_5OH is used (compared to H_2O).[33,34] Further, in case of H_2O, 100% selectivity in H_2O_2 production was observed (**Figure 4.12b**). However, when C_2H_5OH was used, the reaction lost its selectivity. Along with H_2O_2, mixture of CH_3CHO and CH_3COOH was also formed. With increase in H_2O gradient in the mixtures of C_2H_5OH/H_2O, selectivity of H_2O_2 production also increases. Thus, the results clearly suggest that photo-reaction of C_2H_5OH with increasing H_2O gradient at around room temperature promotes selective H_2O_2 production, while that of H_2O with increasing C_2H_5OH gradient increases H_2O_2 yield. The study also reveals the effect of amount of CD in the polymer matrix on H_2O_2 production (**Figure 4.12c**). It was found that in a 50 h photo-reaction, production of H_2O_2 increases with increase amount of CD content up to 4 wt% (PNC1.0-PNC4.0). However, beyond 5 wt% (PNC5.0) production of H_2O_2 start to decrease slightly. This might happened because of agglomeration of CD at higher loading, which reduced its light harvesting activity. Reusability test also reveals good result for the nanocomposite system as heterogeneous catalyst (**Figure 4.12d**).

Such photo-catalytic activity of the nanocomposite is significant. Because, sustainable, safe and green production of H_2O_2 is very important due to its role as a green oxidant (leaves H_2O as the only by-product) and energy carrier for fuel cell (H_2O_2 can be used in one compartment fuel cell with out-put potential of 1.09 V). Various metal based semi-conductors have been reportedly utilized for sustainable production of H_2O_2 using H_2O and alcohol. These include Ru-complex, TiO_2 etc.[35-38]
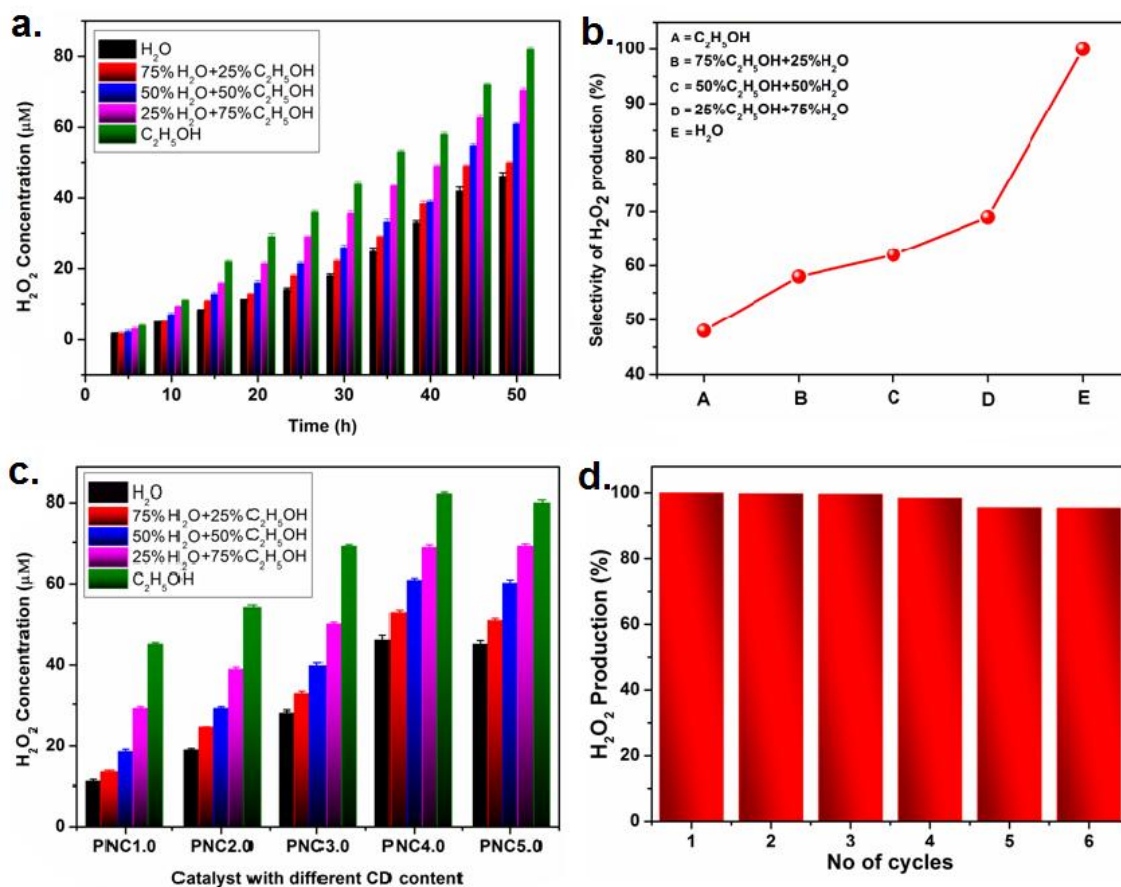
Figure 4.12. (a) H_2O_2 production with different materials at different time intervals using PNC4.0 as catalyst, **(b)** Selectivity curve of H_2O_2 production with different starting materials (using PNC4.0 as catalyst), **(c)** Effect of CD loading on H_2O_2 production (after 50 h of reaction) and **(d)** Reusability of the catalyst (PNC4.0).

But most of these catalysts are associated with the concerns of high cost, toxicity, metal based origin and non-biodegradable nature. In this context, present system can claim superiority by virtue of facile preparative method, biodegradability and non-toxic behavior.

4.4. Conclusion

Thus, the present study demonstrated successful *in situ* and *ex situ* fabrication of waterborne hyperbranched polyurethane/carbon dot nanocomposites. The study witnessed improvement of various material properties of the pristine polymer after the formation of nanocomposite. Incorporation of carbon dot leads to the enhancement of mechanical properties and thermal stability of the original polymer. Carbon dot by virtue of its typical behavior imparts fascinating optical properties to

the nanocomposite system. The nanocomposite films exhibited multi-color emission under different wavelengths of light, which can be used to design high security mark along with other opto-electronic devices. On the other hand, nanocomposite films were effectively used as heterogeneous catalyst for solar driven hydrogen peroxide production. Such an approach may open avenue for polymer supported carbon dot as catalyst in different photo reactions. The biological assessment, particularly osteoblast proliferation revealed a cytocompatible material which has the potentiality to be used in allied biomedical applications. Enhanced osteoblast differentiation capability of the nanocomposite indicates suitability of carbon dot impregnated polyurethane matrix for bone tissue engineering applications. Over all, the study showed waterborne hyperbranched polyurethane/carbon dot nanocomposite as a high performance, luminescent, cytocompatible material with profound photo-catalytic activity.

References

(1) Paul, D.R., & Robeson, L.M. Polymer nanotechnology: Nanocomposites, *Polymer* **49**, 3187--3204, 2008.

(2) Koo, J.H. *Polymer Nanocomposites*, McGraw-Hill, New York, 2006.

(3) Scholz, M.S., et al. The use of composite materials in modern orthopaedic medicine and prosthetic devices: A review, *Compos. Sci. Technol.* **71**, 1791--1803, 2011.

(4) Kuan, H.C., et al. Synthesis thermal mechanical and rheological properties of multiwall carbon nanotube/waterborne polyurethane nanocomposite, *Compos. Sci. Technol.* **65**, 1703--1710, 2005.

(5) Ramanathan, T., et al. Functionalized graphene sheets for polymer nanocomposites, *Nat. Nanotechnol.* **3**, 327--331, 2008.

(6) Hussain, F., et al. Polymer matrix nanocomposites, processing, manufacturing, and application: An overview, *J. Compos. Mater.* **40**, 1511--1575, 2006.

(7) Neuberger, T., et al. Superparamagnetic nanoparticles for biomedical applications: Possibilities and limitations of a new drug delivery system, *J. Magn. Magn. Mater.* **293**, 483--496, 2005.

(8) Mauter, M.S., & Elimelech, M. Environmental applications of carbon-based nanomaterials, *Environ. Sci. Technol.* **42**, 5843--5859, 2008.

(9) Du, F., et al. Economical and green synthesis of bagasse-derived fluorescent carbon dots for biomedical applications, *Nanotechnology* **25**, 315702, 2014.

(10) Lim, S.Y., et al. Carbon quantum dots and their applications, *Chem. Soc. Rev.* **44**, 362--381, 2015.

(11) Bacon, M., et al. Graphene quantum dots, *Part. Part. Syst. Charact.* **31**, 415--428, 2014.

(12) Baker, S.N., & Baker, G.A. Luminescent carbon nanodots: emergent nanolights, *Angew. Chem. Int. Ed.* **49**, 6726--6744, 2010.

(13) Sk, M.P., et al. Presence of amorphous carbon nanoparticles in food caramels, *Sci. Rep.* **2**, 383, 2012.

(14) Wang, H.X., et al. Rational design of nitrogen and sulfur co-doped carbon dots for efficient photoelectrical conversion applications, *J. Mater. Chem. A* **3**, 11287--11293, 2015.

(15) KyungaJung, Y. Sweet nanodot for biomedical imaging: carbon dot derived from xylitol, *RSC Adv.* **4,** 23210--23213, 2014.

(16) Narayanan, R., et al. Forster resonance energy transfer and carbon dots enhance light harvesting in a solid-state quantum dot solar cell, *J. Mater. Chem. A* **1**, 3907--3918, 2013.

(17) De, B., & Karak, N. A green and facile approach for the synthesis of water soluble fluorescent carbon dots from banana juice, *RSC Adv.* **3**, 8286--8290, 2013.

(18) Zhou, L., et al. Amphibious fluorescent carbon dots: one-step green synthesis and application for light-emitting polymer nanocomposites, *Chem. Commun.* **49**, 8078--8080, 2013.

(19) Kwon, W., et al. Freestanding luminescent films of nitrogen-rich carbon nanodots toward large-scale phosphor based white-light-emitting devices, *Chem. Mater.* **25**, 1893--1899, 2013.

(20) Thakur, S., & Karak, N. Green reduction of graphene oxide by aqueous phytoextracts, *Carbon* **50**, 5331--5339, 2012.

(21) Mandal, B.B., & Kundu S.C. Osteogenic and adipogenic differentiation of rat bone marrow cells on non-mulberry and mulberry silk gland fibroin 3D scaffolds, *Biomaterials* **30**, 5019--5030, 2009.

(22) Mandal, B.B., & Kundu, S.C. Non-mulberry silk gland fibroin protein 3-D scaffold for enhanced differentiation of human mesenchymal stem cells into osteocytes, *Acta Biomater.* **5**, 2579--2590, 2009.

(23) Tsukamoto, D., et al. Selective photocatalytic oxidation of alcohols to aldehydes in water by TiO_2 partially coated with WO_3, *Chem.-Eur. J.* **17**, 9816--9824, 2011.

(24) Hussain, M., et al. Composition and nutritive value of cormels of Colocasia esculenta (L.) Schott, *J. Sci. Food Agric.* **35**, 1112--1119, 1984.

(25) Sahu, S., et al. Simple one-step synthesis of highly luminescent carbon dots from orange juice: application as excellent bio-imaging agents, *Chem. Commun.* **48**, 8835--8837, 2012.

(26) Ryu, J., et al. Hydrothermal preparation of carbon microspheres from mono-saccharides and phenolic compounds, *Carbon* **48**, 1990--1998, 2010.

(27) Mewada, A., et al. Non-blinking dendritic crystals from C-dot solution, *Carbon Lett.* **16**, 211--214, 2015.

(28) De, B., et al. Transparent luminescent hyperbranched epoxy/carbon oxide dot nanocomposites with outstanding toughness and ductility, *ACS Appl. Mater. Interfaces* **5**, 10027--10034, 2013.

(29) Liu, Y., et al. Chemical cross-linking modification of polyimide membranes for gas separation, *J. Membr. Sci.* **189**, 231--239, 2001.

(30) Stevenson, A.T., et al. Fabrication and characterization of medical grade polyurethane composite catheters for near-infrared imaging, *Biomaterials* **54**, 168--176, 2015.

(31) Yang, S.T., et al. Carbon dots as nontoxic and high-performance fluorescence imaging agents, *J. Phys. Chem. C* **113**, 18110--181114, 2009.

(32) Hsu, P.C., et al. Synthesis and analytical applications of photoluminescent carbon nanodots, *Green Chem.* **14**, 917--920, 2012.

(33) Shiraishi, Y., et al. Sunlight-driven hydrogen peroxide production from water and molecular oxygen by metal-free photocatalysts, *Angew. Chem*. **126**, 13672--3677, 2014.

(34) Shiraishi, Y., et al. Highly selective production of hydrogen peroxide on graphitic carbon nitride (g-C_3N_4) photocatalyst activated by visible light, *ACS Catal.* **4**, 2014, 774--780.

(35) Isaka, Y., et al. Bottom-up and top-down methods to improve catalytic reactivity for photocatalytic production of hydrogen peroxide using a Ru-complex and water oxidation catalysts, *J. Mater. Chem. A* **3**, 12404--12412, 2015.

(36) Kormann, C., et al. Photocatalytic production of hydrogen peroxides and organic peroxides in aqueous suspensions of titanium dioxide, zinc oxide, and desert sand, *Environ. Sci. Technol.* **22**, 798--806, 1988.

(37) Cai, R., et al. Effect of copper ions on the formation of hydrogen peroxide from photocatalytic titanium dioxide particles, *J. Catal.* **219**, 214--218, 2003.

(38) Goto, H., et al. Quantitative analysis of superoxide ion and hydrogen peroxide produced from molecular oxygen on photoirradiated TiO_2 particles, *J. Catal.* **225**, 223--229, 2004.